



# Enhancing water splitting activity by protecting hydrogen evolution activity site from poisoning of oxygen species

Bin Tian<sup>a,b</sup>, Wei Gao<sup>a,b</sup>, Xiaofeng Ning<sup>a,b</sup>, Yuqi Wu<sup>a</sup>, Gongxuan Lu<sup>a,\*</sup>

<sup>a</sup> State Key Laboratory for Oxo Synthesis and Selective Oxidation Lanzhou Institute of Chemical Physics, Chinese Academy of Sciences, Lanzhou, 730000, China

<sup>b</sup> University of Chinese Academy of Sciences, Beijing, 100049, China

## ARTICLE INFO

### Key words:

Over-all water splitting  
Visible light induced hydrogen evolution  
Poisoning of oxygen species  
Protection of hydrogen evolution activity site

## ABSTRACT

Photocatalytic hydrogen evolution via water splitting is considered as one of ideal ways to solar energy conversion and storage, however, the low energy conversion efficiency and weak catalyst stability are still two main obstacles to overcome. In our present study, we found hydrogen peroxide formed during water splitting affect deleteriously the hydrogen evolution activity of catalyst due to the occupation of active sites on catalyst. Such a negative effect of hydrogen peroxide on hydrogen generation can be prohibited by introduction of superoxide dismutase (SOD), which is able to decompose the adsorbed hydrogen peroxide. The in-situ synthesized  $\text{Sn}^{4+}$  center over SnO photocatalyst can catalytically decompose hydrogen peroxide more efficiently than SOD, and as a result,  $\text{Sn}^{4+}/\text{SnO}$  photocatalyst exhibited higher activity for over-all water splitting and better stability. By taking advantage of  $\text{Sn}^{4+}$  catalytic properties for hydrogen peroxide, the rate of  $\text{H}_2$  evolution reached  $18.3 \mu\text{mol} \cdot \text{g}^{-1} \cdot \text{h}^{-1}$  and the corresponding AQE of 0.18% at 420nm over  $\text{Sn}^{4+}/\text{SnO}$  catalyst under visible light irradiation without noble metal loading.

## 1. Introduction

The increasing consumption of fossil fuel leads to the huge amount of greenhouse gas emission, therefore searching the renewable energy resource replacing fossil fuel is one of the most important objectives for our society. One attractive route is the development of hydrogen based energy system, while hydrogen is generated by solar energy, i.e., conversion and storage of solar energy as hydrogen [1–5]. In various strategies, photocatalytic water splitting to hydrogen driven by solar irradiation seems to be one of the best promising routes [6,7]. Efficient photocatalytic water splitting requires catalyst both active for reduction reaction (hydrogen evolution reaction, HER) and oxidation reaction (oxygen evolution reaction, OER) [8]. However, the low energy conversion efficiency due to the weak adsorption of solar irradiation, low excited charge separation efficiency, and unsatisfied catalyst stability impeded photocatalysis application in over-all water splitting. Recently, scientist found nascent formed oxygen species might inhibit hydrogen formation via reverse hydrogen-oxygen recombination or even make catalyst poisoned by occupation of active sites over catalyst, which results in catalyst deactivation [9,10].

In fact, oxygen species poisoning effect is very significant in biological nitrogen fixation (BNF), which is an important route nitrogen cycle in our nature [11,12]. BNF is based on the function of nitrogen-

fixing microorganisms (NFMs), or nitrogenase. It is known that BNF can only take place in a strict anaerobic environment, because the nitrogenase (molybdenum ferritin and ferritin) is extremely sensitive to oxygen [13]. Once exposed to oxygen, nitrogenase deactivates very quickly, thus, these NFMs developed multiple mechanisms to resolve this contradiction, via, (i) intensive respiration consuming the formed oxygen and making enzyme in a low-oxygen ambient, (ii) combination oxygen by leghemoglobin and (iii) formed a mucosal layer preventing oxygen passing through [14–16].

Coincidentally, the same phenomenon were observed in photocatalytic overall water splitting reaction in our recent studies, in particular, the nascent formed oxygen exhibits an adverse effect on hydrogen evolution both in activity and stability of photocatalyst [17]. In our previous work, we found remarkable hydrogen evolution rate promotion by using oxygen transfer reagent or device (such as perfluorodecalin, chlorhematin and artificial gill, etc.) in photocatalytic over-all water splitting [17–19].

We recently found that the nascent formed oxygen intermediate species during water splitting, such as hydrogen peroxide, impeding deleteriously the hydrogen evolution in water splitting. In this work, we develop a strategy to overcome this negative effect by introduction of superoxide dismutase (SOD), which is able to decompose the adsorbed hydrogen peroxide. In addition, the in-situ fabricated  $\text{Sn}^{4+}$  center over

\* Corresponding author.

E-mail address: [gxlu@lzb.ac.cn](mailto:gxlu@lzb.ac.cn) (G. Lu).

<https://doi.org/10.1016/j.apcatb.2019.02.051>

Received 12 December 2018; Received in revised form 13 February 2019; Accepted 18 February 2019

Available online 01 March 2019

0926-3373/© 2019 Elsevier B.V. All rights reserved.

SnO photocatalyst can catalytically decompose nascent formed hydrogen peroxide. As a result,  $\text{Sn}^{4+}/\text{SnO}$  photocatalyst exhibited higher activity for over-all water splitting and better stability. By taking advantage of  $\text{Sn}^{4+}$  catalytic properties for hydrogen peroxide, the  $\text{H}_2$  evolution rate of  $18.3 \mu\text{mol g}^{-1} \text{h}^{-1}$  and the corresponding AQE of 0.18% at 420 nm over  $\text{Sn}^{4+}/\text{SnO}$  catalyst have been achieved under visible light irradiation without any noble metal loading.

## 2. Experimental section

### 2.1. Materials

All chemicals were analytic pure and used without further purification. Stannous chloride ( $\text{SnCl}_2 \cdot 2\text{H}_2\text{O}$ , Tianjin Kemiou Chemical Reagent Co., Ltd, AR,  $\geq 99.5\%$ ), stannic chloride ( $\text{SnCl}_4 \cdot 5\text{H}_2\text{O}$ , Tianjin Kemiou Chemical Reagent Co., Ltd, AR,  $\geq 99.5\%$ ), commercial stannic oxide ( $\text{SnO}_2$ , Sinopharm Chemical Reagent Co. Ltd.,  $\geq 98.0\%$ ), ethanediamine ( $\text{C}_2\text{H}_8\text{N}_2$ , Sinopharm Chemical Reagent Co. Ltd.,  $\geq 98.0\%$ ), ammonium thiocyanate ( $\text{NH}_4\text{SCN}$ , Beijing shuanghuan chemical reagent plant,  $\geq 98.5\%$ ), ferrous chloride ( $\text{FeCl}_2 \cdot 4\text{H}_2\text{O}$ , Xilong Scientific Co., Ltd.,  $\geq 98.0\%$ ), perfluorodecalin (Sinopharm Chemical Reagent Co. Ltd.,  $\geq 99.5\%$ ). De-ionized water with a specific resistance of  $18.2 \text{ M } \Omega \cdot \text{cm}^{-2}$  was obtained by reverse osmosis followed by ion-exchange and filtration (RFD 250NB, Toyo Seisakusho Kaisha, Ltd., Japan).

### 2.2. Preparation of SnO and $\text{Sn}^{4+}$ -SnO nanosheets

The  $\text{Sn}^{4+}$ -SnO photocatalyst was prepared by solvothermal method used  $\text{SnCl}_4 \cdot 5\text{H}_2\text{O}$ ,  $\text{SnCl}_2 \cdot 2\text{H}_2\text{O}$  and ethanediamine as raw materials. As shown in Fig. S1, the typical synthesis procedure of  $\text{Sn}^{4+}$ -SnO photocatalyst is as follow: a certain amount of stannous chloride and stannic chloride was dissolved in ethanediamine under strong stirring. The mix solution was then transferred into a 50 mL teflon-lined stainless steel autoclave and kept at certain temperature (100, 120, 140, 160 and 180 °C) for 12 h, and cooled down to room temperature naturally. The synthesized sample was separated by suction filtration and washed with benzene, ethanol and water each for three times. Finally, the obtained product was dried at 60 °C for overnight in vacuum oven. The different ratio  $\text{Sn}^{4+}$  sample were prepared by variation of the amount of  $\text{SnCl}_4$ .

### 2.3. Hydrogen evolution activity and apparent quantum efficiency (AQE) tests

The measurements of the photocatalytic  $\text{H}_2$  evolution activity were performed in a sealed Pyrex flask (180 mL) with a flat window (an efficient irradiation area of  $10.2 \text{ cm}^2$ ) and a silicone rubber septum for sampling. Pristine SnO and  $\text{SnO}_2$  were used for comparison. 50 mg photocatalyst was dispersed into 100 mL of pure water under the ultrasound treatment about 2 min, 2 mL perfluorodecalin (PFDL) were added in mix solution under stirring conditions for 30 min. The light source is a 300 W Xenon lamp, which equipped with a 420 nm cutoff filter. Prior to irradiation, the reactant mixture solution was degassed by bubbling Ar gas for 30 min. The amount of hydrogen evolution was measured using gas chromatography (Aglient 6820, TCD,  $13 \times$  column, Ar carrier). The AQE was measured under the same photocatalytic reaction conditions with irradiation light through a band-pass filter (430, 460, 490, 520, 550 and 590 nm). Photon flux of the incident light was determined using a ray virtual radiation actinometer (FU 100, silicon ray detector, light spectrum, 400–700 nm; sensitivity,  $10\text{--}50 \mu\text{V} \mu\text{mol}^{-1} \text{m}^{-2} \text{s}^{-1}$ ). The reaction solutions were irradiated for 1 h with bandpass filters for AQE measurements on the  $\text{H}_2$  evolution. The following equation was used to calculate the AQE.

$$\text{AQE} = \frac{2 \times \text{the number of evolved hydrogen molecules}}{\text{the number of incident photons}} \times 100\%$$

### 2.4. Preparation of working electrodes and electrochemical measurements

All the electrochemical measurements were measured on an electrochemical analyzer (CHI660E) in a typical three-electrode cell (a Pt counter electrode, a reference electrode of saturated Ag/AgCl electrode and a working electrode). The working electrodes were prepared by drop-coating sample suspensions directly onto the precleaned indium tin oxide glass (ITO glass) surface. In detail, composite catalysts powder (2 mg) were dispersed into 1 mL pure water and ultrasonic treatment for 30 min. 75  $\mu\text{L}$  sample mixture was drop-coated onto the precleaned indium tin oxide (ITO) glass or glassy carbon electrode (GCE) surface ( $0.016 \text{ cm}^2$ ) and was air-dried (loaded about  $0.15 \text{ mg} \cdot \text{cm}^{-2}$ ) before measurement. The supporting electrolyte was  $0.5 \text{ mol} \cdot \text{L}^{-1} \text{H}_2\text{SO}_4$  aqueous solutions. The interfacial charge transfers of catalysts were exposed using the electrochemical impedance spectroscopies (EIS) in the frequency range of  $10^{-2}$  to  $10^6 \text{ Hz}$  with 10 mV sinusoidal perturbations. The Mott-Shottky curves were obtained by impedance-potential technology with a fix frequency of 1000 Hz A 300 W Xe lamp equipped with an optical cutoff filter of 420 nm was used for excitation.

### 2.5. Characterizations

X-ray diffraction (XRD) data were obtained on a Rigaku B/Max-RB diffractometer with a nickel filtrated  $\text{Cu K}\alpha$  radiation operated at 40 kV and 40 mA over a  $2\theta$  range of  $10\text{--}80^\circ$  and a position sensitive detector using a step size of  $0.017^\circ$  and a step time of 15 s. Transmission electron microscopy (TEM) and high-resolution TEM (HRTEM) images were recorded using a Tecnai-G2-F30 field emission transmission electron microscope with an accelerating voltage of 300 kV. X-ray photoelectron spectroscopy (XPS) analysis was implemented on a VG Scientific ESCALAB 210-XPS with a Mg  $\text{K}\alpha$  X-ray resource. The binding energy C 1 s peak from surface adventitious carbon (284.7 eV) was adopted as a reference for the binding energy measurements. The UV–vis spectra were obtained with a Shimadzu UV-3600 UV–vis-IR spectrophotometer and TU-1900 double beam UV–vis spectrophotometer. Micro-Raman spectra were obtained using a LabRam HR800 Jobin-Yvon spectrometer with an excitation wavelength of 633 nm. The isotopes tracer experiments were carried out via the mass spectrometer with a type of Tilon. The electrochemical characterizations were carried out via an electrochemical analyzer (CHI660E) in a typical three-electrode cell.

## 3. Results and discussion

The OER as a multi-electrons process requires large overpotential to overcome the kinetic barrier for these multistep processes, which also easy to induce kinetically competitive reactions, e.g. the formation reaction of peroxide hydrogen [20,21]. Grätzel's group found that peroxo complexes,  $-\text{Ti}-\text{O}-\text{O}-\text{Ti}-$ , formed on the surface of  $\text{TiO}_2$  during photocatalytic water splitting reaction [22]. The similar phenomenon was also observed in other semiconductors water splitting system, such as niobates,  $\text{g-C}_3\text{N}_4$  and  $\text{WO}_3$ , etc [23,24]. Further investigation suggests that the formed peroxides have a negative effect on the activity of photocatalysts [24].

In order to ascertain hydrogen peroxide formed in our system, we titrated the reaction solution with a  $\text{Fe}^{2+}$  and  $\text{SCN}^-$  solution after reaction, and measured the maximum absorption peak of  $[\text{Fe}(\text{SCN})]^{2+}$  (475 nm) using UV–vis spectroscopy to detect the hydrogen peroxide content (Supporting information) [25]. As a control, the SnO solution without solar light irradiation was carried out as blank test. As shown in Fig. S2, no obvious peak at 475 nm was observed in blank test, however, in light irradiation system, a small amount of hydrogen peroxide was observed, and the concentration of hydrogen peroxide gradually increased with photoreaction proceeding (Fig. 1). These results provide evidences that hydrogen peroxide formed during photocatalytic hydrogen evolution in SnO catalyzed HER. Thus, some measures should be executed to remove these peroxides from system to regenerate the

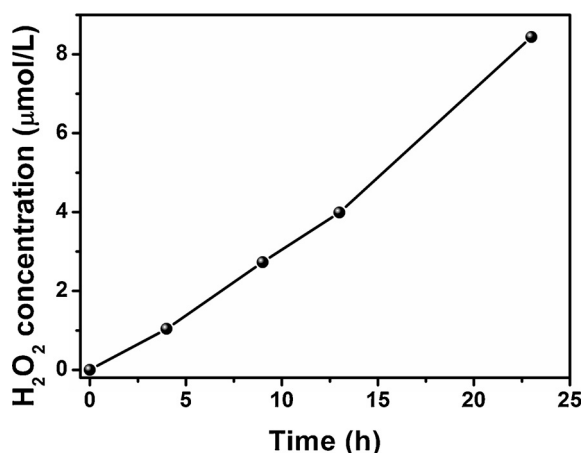


Fig. 1. The time dependence of the hydrogen peroxide concentration over the SnO suspension system during photocatalytic water splitting, the hydrogen peroxide concentration calculated based on absorption intensity.

photocatalysts. It is noted that the potential of water oxidation to hydrogen peroxide is 1.78 V vs. NHE, however, the valence band position of SnO nanosheets is located at 1.58 V vs. NHE (Fig. S3), indicating that the oxidation of water to form hydrogen peroxide by photogenerated holes of SnO is thermodynamically not favored [26]. However, research found that the active sites of catalyst surface have the ability to activate the target compound with lower energy demands [27,28]. In SnO system, it can be speculated that by means of surface activation, water molecules could be oxidized into H<sub>2</sub>O<sub>2</sub> by photoinduced holes.

Furthermore, the photocatalysis hydrogen production experiments at a constant hydrogen peroxide concentration aqueous solution were carried out under visible light irradiation to ascertain the negative effect of hydrogen peroxide for our photocatalytic system. As shown in Fig. 2A, the hydrogen evolution activity decreases significantly after adding H<sub>2</sub>O<sub>2</sub> in SnO system, and the hydrogen evolution activity shows a dependence on the concentration of H<sub>2</sub>O<sub>2</sub>. Such a negative effect of

hydrogen peroxide on hydrogen generation can be reduced by introduction of superoxide dismutase (SOD, Fig. 2B), which is able to decompose the adsorbed hydrogen peroxide. However, the decomposing efficiency of SOD for formation hydrogen peroxide cannot reach our expectation, and thus, we constructed the high valence Sn species as the center of catalytic decompose hydrogen peroxide to enhance the hydrogen evolution activity and stability. As shown in Fig. 2B, it still exhibits the hydrogen evolution activity just shows slight decreases in Sn<sup>4+</sup>-SnO system even though the high hydrogen peroxide concentration.

In order to further ascertain the protect effect of Sn<sup>4+</sup> for hydrogen evolution sites, the oxygen evolution from hydrogen peroxide solution over SnO-based photocatalysts were compared under the same condition. As shown in Fig. 2C, the SnO<sub>2</sub> exhibits higher O<sub>2</sub> production activity than pristine SnO nanosheets in the dark condition, indicating the high valence state of Sn is indeed good for decomposing peroxide hydrogen. Furthermore, the Sn<sup>4+</sup>-SnO photocatalysts exhibit the highest oxygen evolution rate (about 10 times than that of SnO nanosheets, Fig. 2D), which could be attributed to the more active sites of 2D materials [29]. Under the condition of visible light irradiation, the SnO<sub>2</sub> still exhibits higher O<sub>2</sub> production activity than SnO nanosheets, suggesting that Sn<sup>2+</sup> species have a poor hydrogen peroxide decompose activity. The Sn<sup>4+</sup>-SnO system exhibits a higher oxygen activity comparison with dark state, suggesting the decomposition of H<sub>2</sub>O<sub>2</sub> not only is a thermal catalytic process but also a photocatalytic process, which is agreement with our previous report [30].

The time courses of hydrogen evolution catalyzed by SnO and Sn<sup>4+</sup>-SnO in 100 mL pure water under visible light irradiation are shown in Fig. 3A. There was 17.9 μmol g<sup>-1</sup> H<sub>2</sub> in 4 h evolved over SnO photocatalyst under visible light irradiation, however, the Sn<sup>4+</sup>-SnO photocatalyst shows a higher activity for hydrogen evolution, about generate 73.3 μmol g<sup>-1</sup> in 4 h under the same condition. These results suggest the incorporation of Sn<sup>4+</sup> is benefit for catalytically decomposing of formed hydrogen peroxide during water splitting, and protecting hydrogen evolution active sites from the poisoning of H<sub>2</sub>O<sub>2</sub>, and thus resulting in higher hydrogen production activity, finally. In addition,

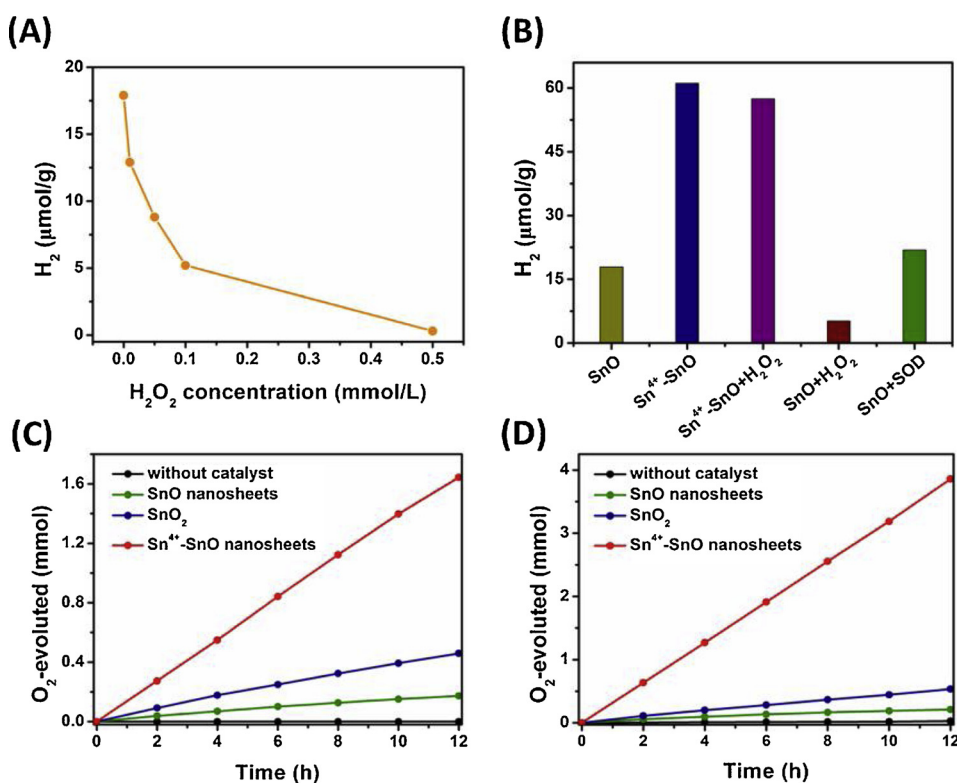
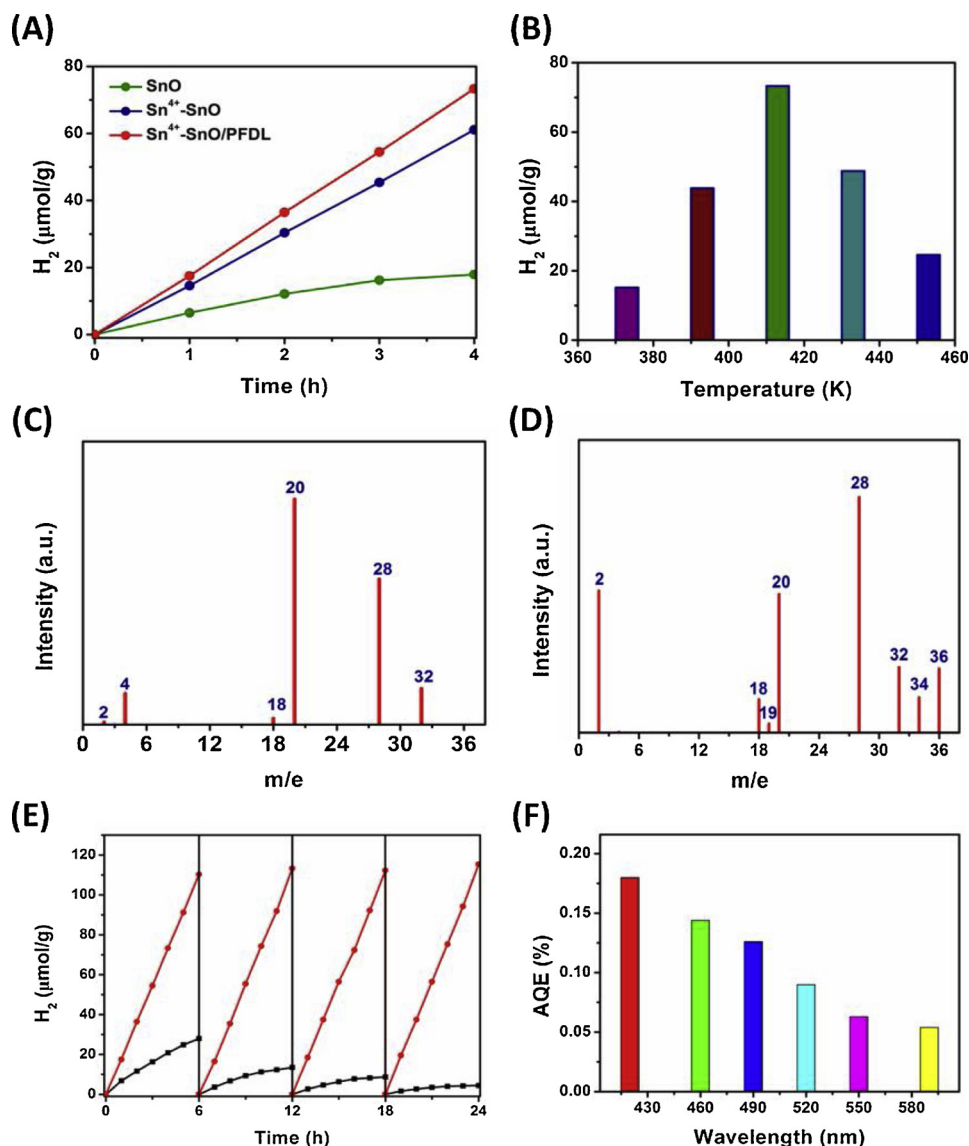


Fig. 2. (A) The time courses of hydrogen evolution activity at different concentration H<sub>2</sub>O<sub>2</sub> aqueous solution. (B) Hydrogen evolution activity comparison of SnO and Sn<sup>4+</sup>-SnO in H<sub>2</sub>O<sub>2</sub> and SOD aqueous solution, the concentration of H<sub>2</sub>O<sub>2</sub> and SOD is 0.1 mmol·L<sup>-1</sup> and 0.1 mg mL<sup>-1</sup>, respectively. The O<sub>2</sub> evolution activity comparison of SnO-based photocatalyst, the solution is 0.5% (wt%) H<sub>2</sub>O<sub>2</sub> aqueous solution, (C) dark state, (D) light irradiation.



**Fig. 3.** (A) Comparison of photocatalytic H<sub>2</sub> evolution with different photocatalysts. (B) Comparison of photocatalytic H<sub>2</sub> evolution with different Sn<sup>4+</sup>-SnO photocatalyst (hydrothermal reaction temperature include 373, 393, 413, 433 and 453 K) under visible light irradiation (λ > 420 nm) at room temperature. The system contains 50 mg photocatalyst, 100 mL deionized water and 2 mL PFDL. The GC-MS spectra obtained after injecting 0.5 mL samples of the gas phase species produced by D<sub>2</sub>O (C) and H<sub>2</sub><sup>18</sup>O (D) over Sn<sup>4+</sup>-SnO/PFDL photocatalytic in a sealed Pyrex flask during visible light irradiation 24 h (λ > 420 nm). (E) Multi-cycle runs for photocatalytic hydrogen evolution in the presence of 50 mg photocatalyst in 100 mL pure water. (F) The apparent quantum yield on Sn<sup>4+</sup>-SnO/PFDL photocatalytic system under monochromatic light irradiation (λ = 420, 460, 490, 520, 550 and 590 nm). Generally, the light source was a Xe lamp (300 W) with a 420 nm long-pass cut filter.

the hydrogen evolution activity shows further enhance after incorporation oxygen capture reagent perfluorodecalin (PFDL), which is attributed to the inhibition of H<sub>2</sub>-O<sub>2</sub> recombination reaction by PFDL [31]. The photocatalytic water splitting activity tests were also carried out to optimize the optimum reaction temperature of preparation Sn<sup>4+</sup>-SnO nanosheets and the results were shown in Fig. 3B. The hydrogen evolution rate reached the maximum when the solvothermal reaction temperature at 413 K, indicated the doping efficiency between Sn<sup>4+</sup> and SnO reached optimal.

The isotopic tracer experiments were then carried out to firmly identify H<sub>2</sub> and O<sub>2</sub> generated via water splitting in Sn<sup>4+</sup>-SnO system, and the results were shown in Fig. 3C and D. Firstly, D<sub>2</sub>O is used to prove the D<sub>2</sub> from water, and the result shows D<sub>2</sub> as the main products are detected, indicated the H<sub>2</sub> comes from water splitting reaction (Fig. 3C). Likewise, the photocatalytic splitting heavy oxygen water (H<sub>2</sub><sup>18</sup>O) experiment shows obvious <sup>18</sup>O<sub>2</sub> signal in mass spectra (Fig. 3D), indicated that the formed O<sub>2</sub> in our system also from water splitting. Further experiments were performed to confirm the photocatalytic stability of the SnO nanosheets after introduction of Sn<sup>4+</sup>. The reaction system was evacuated every 6 h and the process was carried out for repeated cycles. As shown in Fig. 3E, it is clearly seen that the bare SnO shows rather poor stability under visible light irradiation. Typically, the hydrogen production activity in bare SnO system shows

obviously decrease after 6 cycles (24 h), as comparison, the Sn<sup>4+</sup>-doped SnO exhibits excellent photocatalytic activity under the same condition, which can further confirm the Sn<sup>4+</sup> doped play an important role in enhancement the stability of SnO photocatalyst. In addition, the AQE for H<sub>2</sub> production was determined for the photocatalytic system. The solution was irradiated with different wavelength visible light irradiation (λ = 420, 460, 490, 520, 550 and 590 nm) and the results were shown in Fig. 3F. The high AQEs of 0.18% at 420 nm and 0.054% at 590 nm for hydrogen generation are achieved, which is agreement with UV-vis spectra of photocatalysts (Fig. S3). Efficient conversion of visible light energy suggests that the present Sn<sup>4+</sup>-SnO/PFDL photocatalytic system is an effective photocatalytic system for hydrogen evolution and the Sn<sup>4+</sup> play an important role in this process.

To unveil the mechanism responsible for the significantly enhanced photocatalytic H<sub>2</sub> evolution of Sn<sup>4+</sup>-SnO relative to the pristine SnO nanosheets, a series of morphological and spectroscopic characterizations were carried out. As shown in Fig. 4, the morphologies and component of photocatalysts were firstly observed by TEM. The typical TEM image (Fig. 4A) shows that Sn<sup>4+</sup>-SnO photocatalysts have a sheet structure with a size of about 50 nm, thickness of about 2 nm (Fig. S4), which is consistent with about 2–3 atomic layer thickness reports in literature [32].

Furthermore, the HRTEM experiments are carried out to ascertain



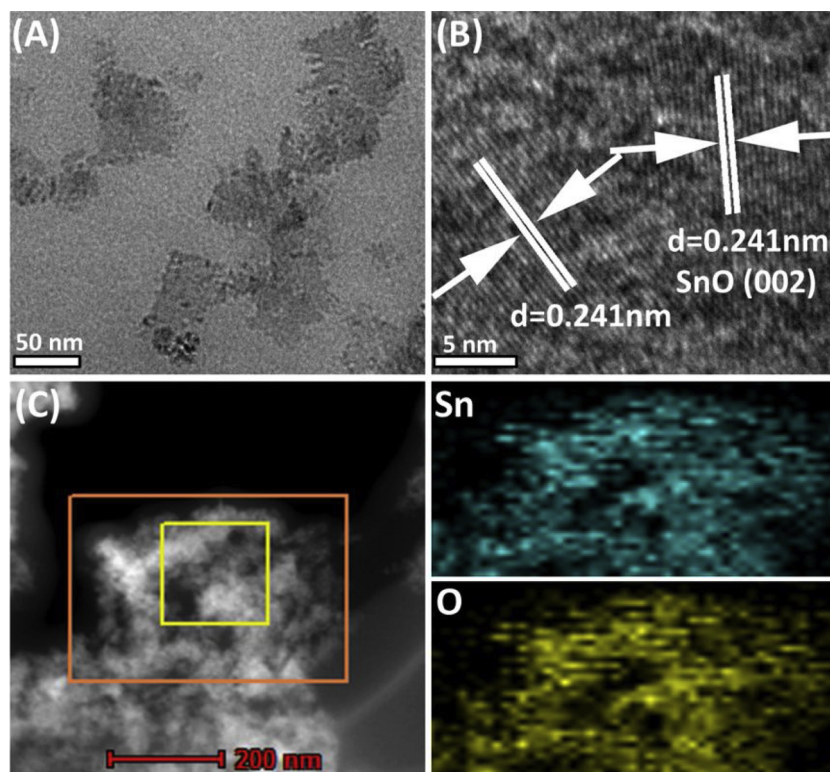


**Fig. 4.** The morphology characterization of  $\text{Sn}^{4+}$ -SnO samples. (A) and (B) the TEM and HRTEM images of  $\text{Sn}^{4+}$ -SnO photocatalyst, (C) the element mapping of  $\text{Sn}^{4+}$ -SnO nanosheets.

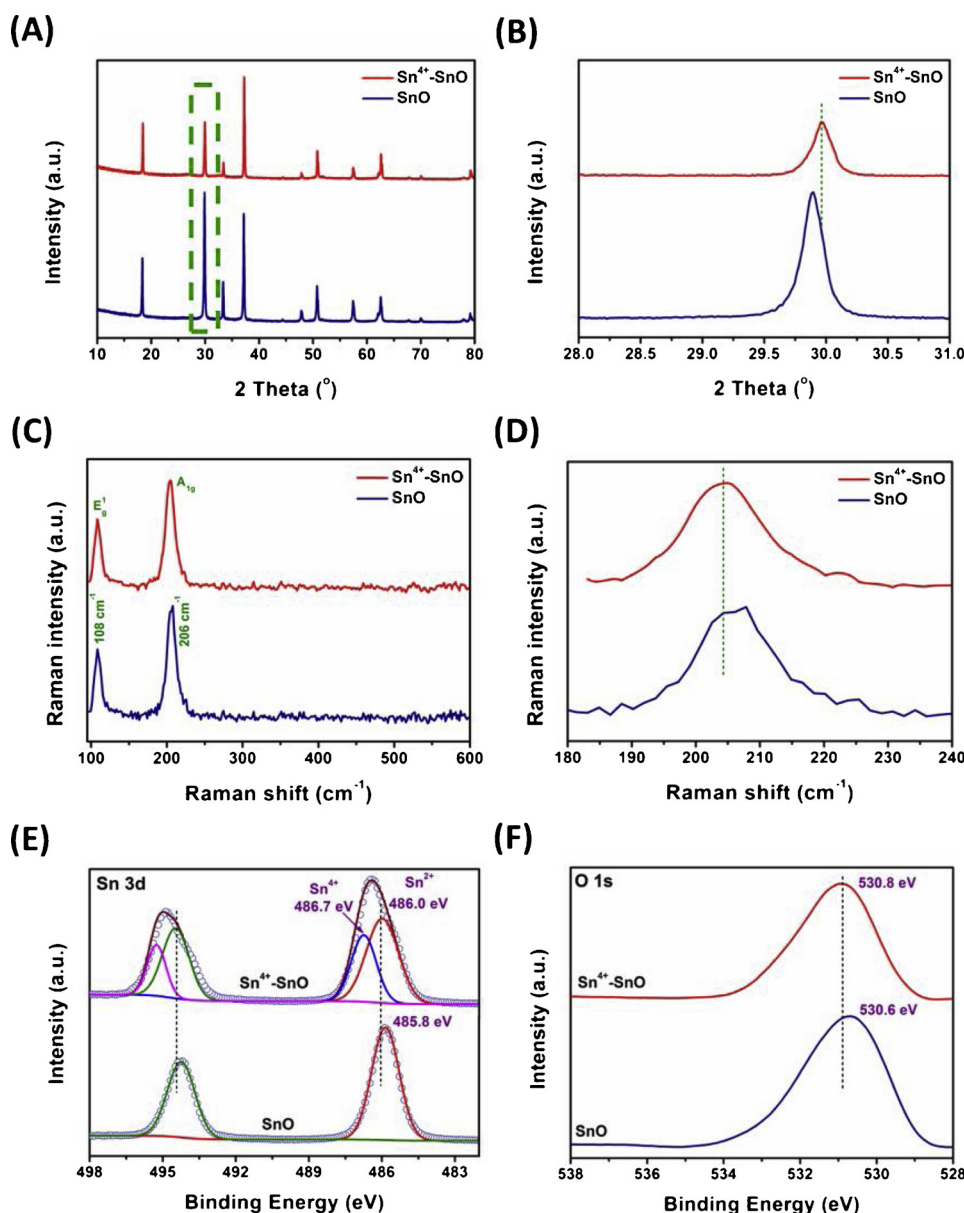
the phase and species of as-prepared samples and shown in Fig. 4B, the image of sample shows a clear lattice spacing of approximately 0.241 nm, indicating a good crystalline and corresponding to the (002) plane of hexagonal SnO. Besides, the energy dispersive X-ray (EDX) spectroscopy data (Fig. S5) shows the signals of Sn and O, implying the SnO-based photocatalyst is successfully constructed. To further ascertain the composition and element distribution of the photocatalysts, the TEM elemental mapping analysis was tested. The left image in Fig. 4C shows the TEM image of the region where elemental mapping is carried out. The cyan and yellow colors correspond to the mapping of tin and oxygen elements, respectively. It is observed that all two elements existed in the photocatalysts and two elements (Sn and O) uniformly disperse in our samples, and the distributional ranges of Sn and O elements are excellently overlapped, revealing that Sn and O are in the form of oxide in our samples.

Fig. 5A shows the XRD patterns of as-prepared samples. For the pristine SnO nanosheets, all of the characteristic peaks can be indexed as the tetragonal SnO phase with JCPDS no. 85-0712 (space group of  $P4/nmm$ ), and lattice constants are  $a = b = 3.80 \text{ \AA}$  and  $c = 4.84 \text{ \AA}$ . The tetragonal layered crystal structure of SnO is shown in Fig. S6, where a large interlayer spacing can accommodate ion insertion and the layered structure provides two-dimensional pathways along the  $ab$  plane for ion diffusion [33]. The  $\text{Sn}^{4+}$ -SnO samples show all the diffraction peaks of SnO nanosheets. Beyond that, we can find the peak at  $29.8^\circ$  exhibits a slight red shift (Fig. 5B), which could be attributed to the interaction between  $\text{Sn}^{4+}$  and SnO. Furthermore, the Raman spectra of pristine SnO and  $\text{Sn}^{4+}$ -SnO nanosheets are shown in Fig. 5C. The peaks at 108 and  $206 \text{ cm}^{-1}$  correspond to the  $A_{1g}$  and  $E_g^{(1)}$  vibration modes of SnO, respectively. Fig. S7 shows the vibration modes of SnO that are considered in our work. The  $A_{1g}$  mode is the symmetry preserving mode, representing vibration along the  $c$  axis, which means Sn atoms vibrate toward or away from the O plane, while the  $E_g^{(1)}$  mode involves movements in the  $ab$  plane, which means the vibration within each monolayer or the vibration between adjacent monolayers within the  $ab$

plane [34–36]. The peak at  $206 \text{ cm}^{-1}$  in  $\text{Sn}^{4+}$ -SnO Raman spectrum also shows a slight shift similar to XRD results (Fig. 5D). The shift can be assigned to the introduction of  $\text{Sn}^{4+}$ , result in the electron cloud density change of Sn-O bond in pristine SnO and chemical shift subsequently [37]. All these results suggest that the  $\text{Sn}^{4+}$  is doped into SnO nanosheets successfully.

XPS was executed to characterize the surface composition and chemical states of Sn and O elements in  $\text{Sn}^{4+}$ -SnO nanosheets. The XPS survey in Fig. S8 shows that two main elemental of Sn and O in the  $\text{Sn}^{4+}$ -SnO nanosheets. In the high-resolution Sn 3d spectrum (Fig. 5E), the detected peaks can be fitted into two type peaks, indicate that there are two types Sn element in  $\text{Sn}^{4+}$ -SnO nanosheets. The peaks at 486.0 and 494.5 eV in Fig. 5E correspond to the Sn  $3d_{5/2}$  and Sn  $3d_{3/2}$  photoelectron emissions of  $\text{Sn}^{2+}$ , respectively [38]. Furthermore, the binding energy of 486.7 and 495.2 eV is attributed to higher valence state species ( $\text{Sn}^{4+}$ ) [39]. The value is close to the Sn 3d spectrum in  $\text{SnO}_2$  sample (Fig. S9). Furthermore, the binding energy of  $\text{Sn}^{2+}$  in  $\text{Sn}^{4+}$ -SnO nanosheets decreased by 0.2 eV as compared to pristine SnO nanosheets (from 486.0 to 485.8 eV for Sn  $3d_{5/2}$ , and from 494.5 to 494.3 eV for Sn  $3d_{3/2}$ ) further confirm the presence of  $\text{Sn}^{4+}$  dopants in the  $\text{Sn}^{4+}$ -SnO nanosheets. The higher binding energy of Sn 3d by self-doping of  $\text{Sn}^{4+}$  in  $\text{Sn}^{4+}$ -SnO may be attributed to the electrons density change of Sn-O bond to preserve charge neutrality, which is in similar to previous study [40]. The reset of energy level of  $\text{Sn}^{4+}$ -SnO nanosheets may also be result in enhancing the absorption in the visible light region [41]. In Fig. 5F, the binding energy of O 1s located at 530.6 eV is assigned to the bond of Sn-O [42]. Interestingly, the O 1s transition peak also shifted 0.2 eV (from 530.6 to 530.8 eV) after self-doping of  $\text{Sn}^{4+}$ , which is consistent with previous report about transition metal-doped SnO nanomaterials [43].

In order to further study the detailed mechanism of enhancing hydrogen evolution activity by high valence  $\text{Sn}^{4+}$  species, we employ photoelectrochemical and photoluminescence spectra techniques. As shown in Fig. 6A, the photocurrent response files show that the  $\text{Sn}^{4+}$ -



**Fig. 5.** The structure characterization of SnO-based nanosheets: (A) the XRD pattern of SnO and  $\text{Sn}^{4+}$ -SnO nanosheets, (B) the partial enlarged view of dashed boxes in (A), (C) Raman spectra of SnO and  $\text{Sn}^{4+}$ -SnO nanosheets and (D) the partial enlarged view of  $A_{1g}$  peak in (C). The XPS spectra of SnO and  $\text{Sn}^{4+}$ -SnO photocatalyst (E) the Sn 3d fine scan spectrum (F) the O 1s fine scan spectrum.

SnO nanosheets have a higher photocurrent than pristine SnO nanosheets, indicating the efficient charge transfer and separation process in  $\text{Sn}^{4+}$ -SnO system. The results could be attributed to lower electron transfer resistance after doping  $\text{Sn}^{4+}$  compared to pristine SnO. Furthermore, electrochemical impedance spectroscopy (EIS) analysis was performed to understand the different electric conductivity of SnO-based photocatalysts. As shown in Fig. 6B, the inset shows the equivalent circuit model used to fit the experimental data. It can be seen that all the plots exhibit a semicircle in the high-frequency region and a sloped line in the low-frequency region. The  $\text{Sn}^{4+}$ -SnO electrode shows a smaller semicircle, and the charge-transfer resistance  $R_{ct}$  of  $\text{Sn}^{4+}$ -SnO and pristine SnO electrodes are 40 and 112  $\Omega$ , respectively. The lower resistance of  $\text{Sn}^{4+}$ -SnO nanosheets electrode is attributed to the following reasons: on the one hand, after incorporation of  $\text{Sn}^{4+}$ , an electrical conductivity increased resulted in a resistance decrease. On the other hand, after doping  $\text{Sn}^{4+}$ , the thickness of SnO decrease (see Fig. S10) and thinner  $\text{Sn}^{4+}$ -SnO nanosheets result in shorter electron transport distance, which reduces the diffusion length of ions and

improves the electrical conductivity of the electrodes [32]. In addition, the EIS of different amount  $\text{Sn}^{4+}$  doping were also tested and the result showed in Fig. S11. We can find that the electrical conductivity improved with the amount of  $\text{Sn}^{4+}$  increasing firstly and decreasing subsequently, which is consistent with the results of UV-vis spectra results (Fig. S12).

To further understand the catalytic regular of  $\text{Sn}^{4+}$  on water splitting, the cyclic voltammograms (CV) of the SnO and  $\text{Sn}^{4+}$ -SnO electrodes were carried out (cathodic sweep first). As we expected, in Fig. 6C, the peak (-0.26 V) at cathode region in SnO nanosheets CV curves could be attributed to the reduction of  $\text{Sn}^{2+}$  to  $\text{Sn}^0$ . Extra peak center at -0.04 V is observed in  $\text{Sn}^{4+}$ -SnO cathode region, which is assigned to the reduction of  $\text{Sn}^{4+}$  to  $\text{Sn}^{2+}$ . Consistently, the anode region of SnO and  $\text{Sn}^{4+}$ -SnO show the similar two peaks, which is attributed to the oxidation of  $\text{Sn}^0$  to  $\text{Sn}^{2+}$  and  $\text{Sn}^{2+}$  to  $\text{Sn}^{4+}$ , respectively. In addition, there is slight shift of the peak of  $\text{Sn}^{2+}$  ( $\text{Sn}^0$ ) to  $\text{Sn}^0$  ( $\text{Sn}^{2+}$ ) comparison with pristine SnO further confirm the electrons transfer from  $\text{Sn}^{2+}$  to  $\text{Sn}^{4+}$  in  $\text{Sn}^{4+}$ -SnO nanosheets. Then, we employed the

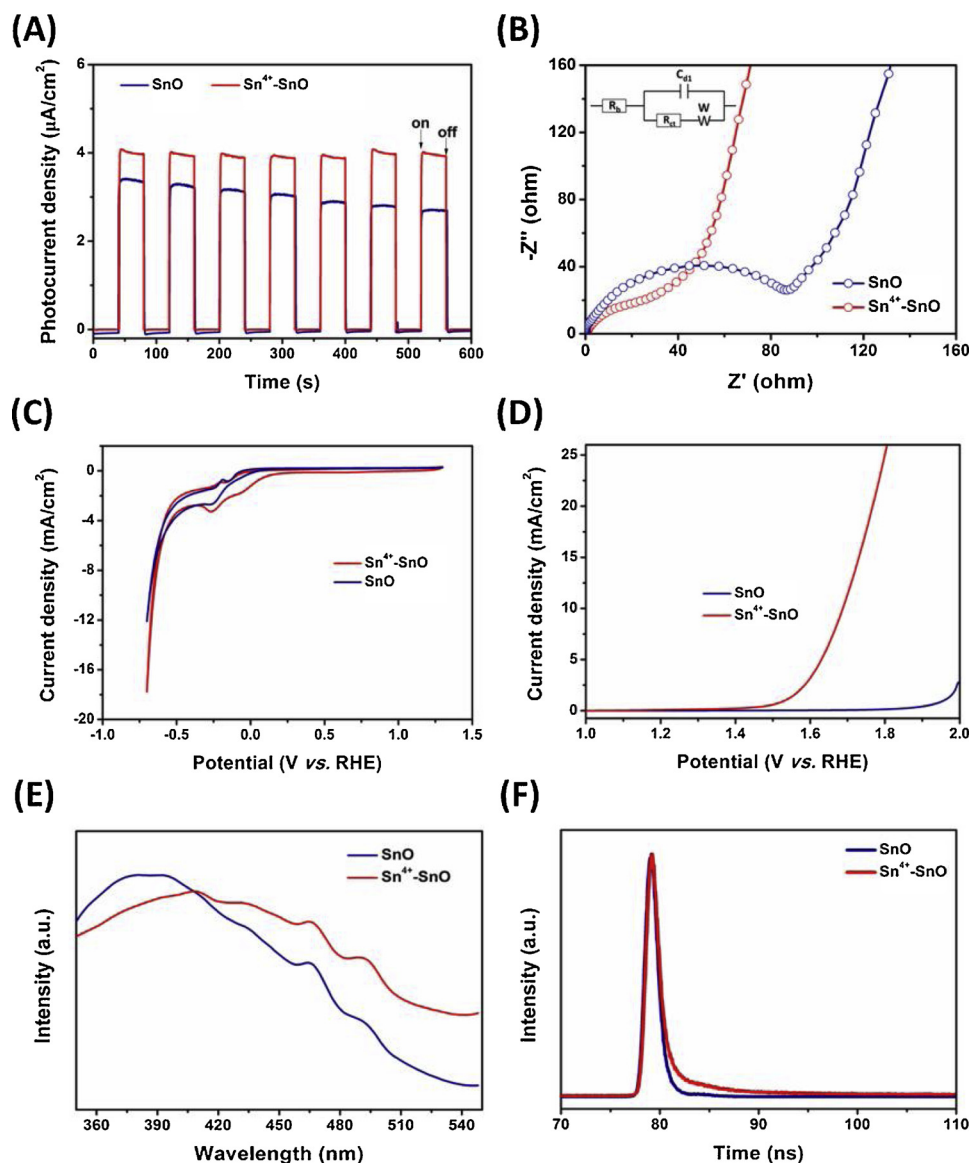
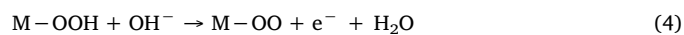
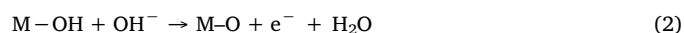
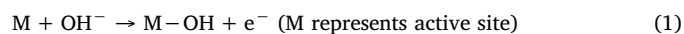


**Fig. 6.** (A) I-t photocurrent response profile of photocatalyst under visible light irradiation ( $\lambda > 420$  nm). (B) Nyquist plots of the SnO and  $\text{Sn}^{4+}$ -SnO electrodes with the corresponding equivalent circuit (inset). (C) Cyclic voltammograms of SnO (navy line)  $\text{Sn}^{4+}$ -SnO (red line) with a scan rates  $10 \text{ mV}\cdot\text{s}^{-1}$  in  $\text{N}_2$  atmosphere. (D) The OER polarization curves of pristine SnO and  $\text{Sn}^{4+}$ -SnO nanosheets. The electrolyte is  $0.1 \text{ mol}\cdot\text{L}^{-1}$  KOH. (E) Photoluminescence spectra of photocatalyst at room temperature and (F) Time-resolved photoluminescence (TRPL) spectra of photocatalyst, the excitation wavelength is 300 nm (For interpretation of the references to colour in this figure legend, the reader is referred to the web version of this article).

linear sweep voltammetry (LSV) curves of hydrogen evolution reaction (HER) and oxygen evolution reaction (OER) to study water splitting activity of SnO-based samples. As shown in Fig. S13, we can find that there is slight overpotential decrease of hydrogen evolution compared SnO and  $\text{Sn}^{4+}$ -SnO nanosheets in HER LSV curves. The change could be attributed to low electron transfer resistance and exposure of the more active site after  $\text{Sn}^{4+}$  doping [44]. It also suggests that  $\text{Sn}^{2+}$  species is hydrogen evolution active center. As we expected, the oxygen evolution overpotential decreased significantly (Fig. 6D) after incorporation  $\text{Sn}^{4+}$  into SnO, indicating that the  $\text{Sn}^{4+}$  strongly influences the OER activity of SnO-based catalyst.

An OER mechanism involving three surface intermediates,  $\text{OH}_{(\text{ad})}$ ,  $\text{O}_{(\text{ad})}$  and  $\text{OOH}_{(\text{ad})}$  has been proposed as follows [45]:



Generally speaking, transition metal cation with a higher valence

state/higher coordination number is benefit for catalyzing water oxidation [46]. In our system, nucleophilic attack of water or  $\text{OH}^-$  occurs on high-oxidation-state  $\text{Sn}(\text{IV})\text{-O}$  intermediates to form the  $\text{O}\cdots\text{O}$  bond, which is similar to the water oxidation process of Cu III species [45]. The reaction kinetics of  $\text{O}-\text{O}$  formation is obviously decreased, resulting in the hydrogen peroxide occupation of active sites on catalyst is weakened, and thus exhibiting higher water splitting activity, subsequently.

Fig. 6E shows the PL data at an excitation wavelength of 300 nm, and two distinct emission bands at about 379 and 392 nm can be observed in SnO system. Also, these emissions are remarkably quenched after doping  $\text{Sn}^{4+}$  in SnO nanosheets, which could be attributed to the effective separation of photoinduced electrons and holes. In addition, obviously red shift is observed in  $\text{Sn}^{4+}$ -SnO system. The red shift could be attributed to the results of the interaction between  $\text{Sn}^{4+}$  and SnO [47]. The efficiently transfer of photogenerated charge carriers of these samples have also been confirmed by the time resolution photoluminescence (TRPL) spectra. As shown in Fig. 6F, the TRPL data further indicated that the lifetime of  $\text{Sn}^{4+}$ -SnO was much longer than that of SnO nanosheets. The decay curves were fitted with two exponentials to obtain the decay time. The results show the SnO nanosheets have an average lifetime about 7.70 ns (Tab. S1). The short decay time



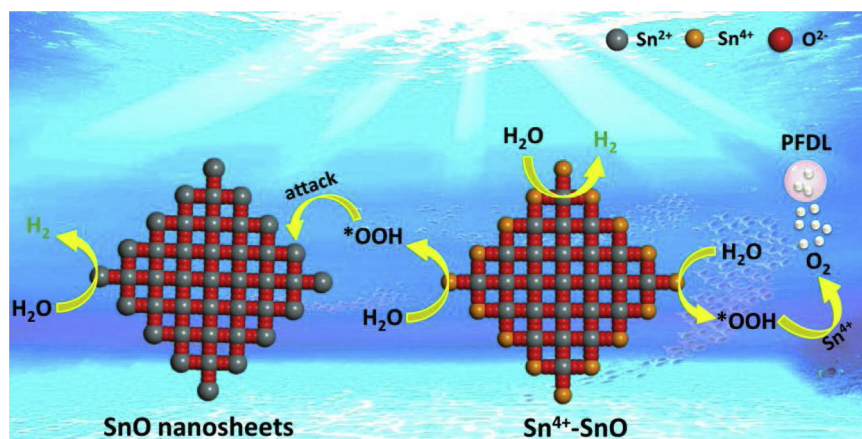


Fig. 7. The mechanism of photocatalytic hydrogen evolution from pure water over  $\text{Sn}^{4+}$ -SnO nanosheets.

component is considered to be due to quasi-free excitons, while the long component is attributed to localized exciton recombination, which is caused by de-trapping of carriers [48]. In contrast, the  $\text{Sn}^{4+}$ -SnO nanosheets have an average decay lifetime (9.37 ns). The much increased lifetime value of  $\text{Sn}^{4+}$ -SnO nanosheets clearly suggests that our photocatalytic system is an effective strategy for the charge transfer and separation, and increases the water splitting activity.

Based on above experiment results and analysis, the whole reaction process of photocatalysis overall water splitting over the  $\text{Sn}^{4+}$ -SnO/PFDL photocatalytic system can be explained in terms of Fig. 7. The enhancement of photocatalytic water splitting activity and stability by  $\text{Sn}^{4+}$  self-doping is mainly attributed to the in-situ synthesized  $\text{Sn}^{4+}$  center over SnO photocatalyst can more efficiently catalyzed decompose hydrogen peroxide. Besides, the increased light absorption, the low electrons transfer resistance and high charge separation efficiency because of doping of  $\text{Sn}^{4+}$  also benefit for hydrogen evolution activity. Thus, the photocatalytic reaction process over  $\text{Sn}^{4+}$ -SnO nanosheets can describe as follow: the semiconductor  $\text{Sn}^{4+}$ -SnO harvests visible light to excite the electrons from the valence band (VB) to the conduction band (CB). The charge carriers transfer to the surface of semiconductors and the electrons reduce  $\text{H}^+$  to generate  $\text{H}_2$  on the surface of photocatalyst, while the  $\text{H}_2\text{O}$  was oxidized via multi-electrons process to form  $\text{O}_2$ . With the assist of  $\text{Sn}^{4+}$ , the formed hydrogen peroxide were catalytically decomposed, and then protecting the hydrogen evolution active sites from poisoning. Meanwhile, the generated  $\text{H}_2$  and  $\text{O}_2$  were then separated by PFDL, resulting in the significant enhanced hydrogen evolution activity and continuous stability, finally.

#### 4. Conclusions

In conclusion, we have determined that the formed hydrogen peroxide during water splitting affected deleteriously the hydrogen evolution activity of catalyst due to the occupation of active sites on catalyst. Such a negative effect of hydrogen peroxide on hydrogen generation can be dramatically reduced by in-situ constructed  $\text{Sn}^{4+}$ -doped SnO photocatalysts. As a result,  $\text{Sn}^{4+}$ -SnO photocatalyst exhibited higher activity for over-all water splitting and better stability. By taking advantage of  $\text{Sn}^{4+}$  catalytic properties for hydrogen peroxide, the rate of  $\text{H}_2$  evolution reached  $18.3 \mu\text{mol g}^{-1} \text{h}^{-1}$  and the corresponding AQE of 0.18% at 420 nm over  $\text{Sn}^{4+}$ /SnO catalysts under visible light irradiation without noble metal loading.

#### Acknowledgement

This work has been supported by the National Natural Science Foundation of China (Grant Nos. 21433007 and 21673262).

#### Appendix A. Supplementary data

Supplementary material related to this article can be found, in the online version, at doi:<https://doi.org/10.1016/j.apcatb.2019.02.051>.

#### References

- [1] H.B. Gray, Nat. Chem. 1 (2009) 7–7.
- [2] N.S. Lewis, D.G. Nocera, Proc. Natl. Acad. Sci. U. S. A. 103 (2006) 15729–15735.
- [3] G.X. Lu, X.Q. Zhang, W.L. Zhen, J. Mol. Catal. (China) 33 (2019) 1–9.
- [4] A. Fujishima, K. Honda, K. Kohayakawa, Nature 238 (1972) 37–38.
- [5] Y.L. Zhou, L. Li, C.L. Yang, Y.Z. Jiao, X.R. Zhang, J. Mol. Catal. (China) 31 (2017) 236–246.
- [6] X.X. Zou, Y. Zhang, Chem. Soc. Rev. 44 (2015) 5148–5180.
- [7] G.X. Lu, B. Tian, J. Mol. Catal. (China) 31 (2017) 101–104.
- [8] T.J. Jacobsson, V. Fjällström, M. Sahlberg, M. Edoff, T. Edvinsson, Energy Environ. Sci. 6 (2013) 3676–3683.
- [9] Q. Wang, S. Okunaka, H. Tokudome, T. Hisatomi, M. Nakabayashi, N. Shibata, T. Yamada, K. Domen, Joule 2 (2018) 1–14.
- [10] M.W. Kanan, D.G. Nocera, Science 321 (2008) 1072–1075.
- [11] J.N. Galloway, F.J. Dentener, D.G. Capone, E.W. Boyer, R.W. Howarth, S.P. Seitzinger, G.P. Asner, C.C. Cleveland, P.A. Green, E.A. Holland, D.M. Karl, A.F. Michaels, J.H. Porter, A.R. Townsend, C.J. Vorosmarty, Biogeochemistry 70 (2004) 153–226.
- [12] D. Kumar, H.D. Kumar, Int. J. Hydrogen Energy 16 (1991) 397–401.
- [13] B.K. Burgess, Chem. Rev. 96 (1996) 2983–3011.
- [14] P. Fay, Microbiol. Rev. 56 (1992) 340–373.
- [15] I. Aranjuelo, G. Molero, G. Erice, J.C. Avice, S. Nogues, J. Exp. Bot. 62 (2011) 111–123.
- [16] X.X. Zou, Y. Zhu, E.L. Pohlmann, J.L. Li, Y.P. Zhang, G.P. Roberts, Microbiol.-SGM 154 (2008) 2689–2699.
- [17] B. Tian, B.J. Yang, J. Li, Z. Li, W.L. Zhen, Y.Q. Wu, G.X. Lu, J. Catal. 350 (2017) 189–196.
- [18] Z. Li, B. Tian, W.L. Zhen, Y.Q. Wu, G.X. Lu, Appl. Catal. B 203 (2017) 408–415.
- [19] B. Tian, Z. Li, W.L. Zhen, X.Q. Zhang, G.X. Lu, J. Catal. 352 (2017) 572–578.
- [20] Y.Y. Liang, Y.G. Li, H.L. Wang, H.J. Dai, J. Am. Chem. Soc. 135 (2013) 2013–2036.
- [21] J.A. Seabold, K.S. Choi, Chem. Mater. 23 (2011) 1105–1112.
- [22] M. Grätzel, Acc. Chem. Res. 14 (1981) 376–384.
- [23] O.C. Compton, E.C. Carroll, J.Y. Kim, D.S. Larsen, F.E. Osterloh, J. Phys. Chem. C 111 (2007) 14589–14592.
- [24] J. Liu, Y. Zhang, L. Lu, G. Wu, W. Chen, Chem. Commun. 48 (2012) 8826–8828.
- [25] R. Shi, H.F. Ye, F. Liang, Z. Wang, K. Li, Y.X. Weng, Z.S. Lin, W.F. Fu, C.M. Che, Y. Chen, Adv. Mater. 30 (2018) 1705941.
- [26] J. Liu, Y. Liu, N. Liu, et al., Science 347 (2015) 970–974.
- [27] S.N. Habisreutinger, L.S. Mende, J.K. Stolarczyk, Angew. Chem. Int. Ed. 52 (2013) 7372–7408.
- [28] H. Li, J. Shang, Z.H. Ai, L.Z. Zhang, J. Am. Chem. Soc. 137 (2015) 6393–6399.
- [29] H.T. Wang, D.S. Kong, P. Johanes, J.J. Cha, G.Y. Zheng, K. Yan, N.A. Liu, Y. Cui, Nano Lett. 13 (2013) 3426–3433.
- [30] Z. Li, C. Kong, G.X. Lu, J. Phys. Chem. C 120 (2016) 56–63.
- [31] B. Tian, W. Gao, X.Q. Zhang, Y.Q. Wu, G.X. Lu, Appl. Catal. B 221 (2018) 618–625.
- [32] L. Liang, Y. Sun, F. Lei, S. Gao, Y. Xie, J. Mater. Chem. A 2 (2014) 10647–10653.
- [33] F. Zhang, J.J. Zhu, D.L. Zhang, U. Schwingenschlogl, H.N. Alshareef, Nano Lett. 17 (2017) 1302–1311.
- [34] D. Su, X. Xie, G. Wang, Chem. - Eur. J. 203 (2014) 192–3197.
- [35] S. Koval, R. Burriel, M. Stachiotti, M. Castro, R. Migoni, M. Moreno, A. Varela, C. Rodriguez, Phys. Rev. B: Condens. Matter Mater. Phys. 60 (1999) 14496.
- [36] X. Wang, F. Zhang, I. Loa, K. Syassen, M. Hanfland, Y.L. Mathis, Phys. Status Solidi B 241 (2004) 3168–3178.
- [37] J. Geurts, S. Rau, W. Richter, F. Schmitte, Thin Solid Films 121 (1984) 217–225.



- [38] B. Cheng, J.M. Russell, W.S. Shi, L. Zhang, E.T. Samulski, *J. Am. Chem. Soc.* 126 (2004) 5972–5973.
- [39] D. Han, B.L. Jiang, J. Feng, Y.D. Yin, W.S. Wang, *Angew. Chem. Int. Ed.* 56 (2017) 7792–7796.
- [40] C. Kong, S.X. Min, G.X. Lu, *Chem. Commun.* 50 (2014) 5037–5039.
- [41] C.M. Fan, Y. Peng, Q. Zhu, L. Lin, R.X. Wang, A.W. Xu, *J. Phys. Chem. C* 117 (2013) 24157–24166.
- [42] H.K. Wang, K.P. Dou, W.Y. Teoh, Y.W. Zhan, T.F. Hung, F.H. Zhang, J.Q. Xu, R.Q. Zhang, A.L. Rogach, *Adv. Funct. Mater.* 23 (2013) 4847–4853.
- [43] X.C. Li, Q.J. Yu, C.L. Yu, Y.W. Huang, R.Z. Li, J.Z. Wang, F.Y. Guo, Y. Zhang, S.Y. Gao, L.C. Zhao, *J. Mater. Chem. A* 3 (2015) 8076–8082.
- [44] J.F. Chang, Y. Xiao, M.L. Xiao, J.J. Ge, C.P. Liu, W. Xing, *ACS Catal.* 5 (2015) 6874–6878.
- [45] D.K. Zhong, D.R. Gamelin, *J. Am. Chem. Soc.* 132 (2010) 4202–4207.
- [46] J.J. Duan, S. Chen, M. Jaroniec, S.Z. Qiao, *ACS Catal.* 5 (2015) 5207–5234.
- [47] W.L. Zhen, H.B. Gao, B. Tian, G.X. Lu, *ACS Appl. Mater. Interfaces* 8 (2016) 10808–10819.
- [48] G.H. Ma, S.H. Tang, W.X. Sun, Z.X. Shen, W.M. Huang, J.L. Shi, *Phys. Lett. A* 299 (2002) 581–585.